Article

Numerical Simulation of 30% Efficient Lead-Free Perovskite CsSnGeI₃-Based Solar Cells

Hussein Sabbah [iD]

College of Engineering and Technology, American University of the Middle East, Kuwait; hussein.sabbah@aum.edu.kw

Abstract: A cesium tin–germanium triiodide (CsSnGeI₃) perovskite-based solar cell (PSC) has been reported to achieve a high-power-conversion efficiency (*PCE* > 7%) and extreme air stability. A thorough understanding of the role of the interfaces in the perovskite solar cell, along with the optimization of different parameters, is still required for further improvement in *PCE*. In this study, lead-free CsSnGeI₃ PSC has been quantitatively analyzed using a solar cell capacitance simulator (SCAPS–1D). Five electron transport layers (ETL) were comparatively studied, while keeping other layers fixed. The use of SnO₂ as an ETL, which has the best band alignment with the perovskite layer, can increase the power conversion efficiency (*PCE*) of PSC by up to 30%. The defect density and thickness of the absorber layer has been thoroughly investigated. Results show that the device efficiency is highly governed by the defect density of the absorber layer. All the PSCs with a different ETL exhibit *PCE* exceeding 20% when the defect density of the absorber layer is in the range of 10^{14} cm^{-3}–10^{16} cm^{-3}, and degrade dramatically at higher values. With the optimized structure, the simulation found the highest *PCE* of CsSnGeI₃-based PSCs to be 30.98%, with an open circuit voltage (V_{oc}) of 1.22 V, short-circuit current density (J_{sc}) of 28.18 mA·cm^{-2}, and fill factor (*FF*) of 89.52%. Our unprecedented results clearly demonstrate that CsSnGeI₃-based PSC is an excellent candidate to become the most efficient single-junction solar cell technology soon.

Keywords: solar cell; photovoltaics; thin films; SCAPS simulation; lead-free perovskite; power conversion efficiency; electron transport layer

1. Introduction

Energy consumption is expected to increase, with the bulk of the demand coming from developing countries. Conventional fuel remains the greatest contributor to electricity generation worldwide. Producing energy from these resources takes a severe toll on our environment. Solar energy is one of the most abundant energy resources on Earth, as it is sustainable and inexhaustible. Solar cells are regarded as clean and sustainable sources of energy [1,2]. Coupled with an efficiency rating of greater than 15%, they are a great energy resource [3,4]. To date, conventional silicon (C–Si) solar cells enjoy a market share exceeding 90% of the overall photovoltaic market [5], due to silicon's high stability and power conversion efficiency (*PCE*). Theoretically, the room-temperature power conversion efficiency of a single junction C–Si solar cell is limited to 32.33% [6]. Kaneka Corporation achieved a real-world solar cell with 26.7% conversion efficiency [7,8]. However, there are several drawbacks, namely high cost, difficult preparation conditions, serious environmental pollution [9], and the indirect nature of its electronic band gap, making it a relatively weak absorber of long wavelength sunlight [10].

A decade ago, lead halide Perovskite solar cells (PSCs) emerged as a breakthrough photovoltaic (PV) technology. These cells have acquired significant interest in research and industrial communities due to their high-power-conversion efficiency exceeding 25% [11–13], straightforward fabrication process, and relatively low cost [14,15]. The state-of-the-art certified *PCE* of PSC in single junction architectures exceeded 25% in less than 10 years [16,17],

owing to its tunable direct bandgap, high absorption coefficient, low exciton binding energy, and high carrier mobility [18–21]. Although the perovskite community has put great efforts into addressing the peculiar physics and chemistry of these materials, and has achieved remarkable results, the toxicity of lead associated with the lifecycle of these PSCs is a major concern, hindering their commercialization and future large-scale applications. To conquer this issue, scientists have devoted huge efforts to substitute lead with non-toxic metals such as tin, bismuth, and germanium [22–25].

Tin-based halide perovskites, such as $CsSnI_3$, $CH_3NH_3SnI_3$ ($MASnI_3$), and $HC(NH_2)_2SnI_3$ ($FASnI_3$), have been investigated. The latter two perovskites have intrinsically low stability [26,27]. The all-inorganic lead-free $CsSnI_3$ perovskite could be a promising alternative to Pb-based light harvesting materials, due to its improved photoelectric characteristics such as a high absorption coefficient, small exciton binding energy, high carrier mobility, etc., and is currently the strongest candidate [28–31]. Recently, several studies showed that the substitution of the organic cation by cesium (Cs) in the perovskite structure could significantly enhance its thermal stability and outdoor/ambient device performance [32,33]. Among all lead-free all-inorganic PSCs, $CsSnI_3$ recorded the highest *PCE* of 10.1% [34,35]. Min Chen et al. [36] proposed a perovskite absorber material $CsSnGeI_3$ that shows superior performance and exceptional air stability over its pure counterparts $CsSnI_3$ and $CsGeI_3$. The $CsSnGeI_3$-based device shows a *PCE* of 7%.

This study aims to suggest possible optimization routes for efficiency improvements of the $CsSnGeI_3$ perovskite solar cell, by analyzing various device parameters using a solar cell capacitance simulator (SCAPS-1D) [37]. Different types of simulation software exist, to study the perovskite solar cell performance via computational investigation, such as SIL-VACO ATLAS, AMPS, COMSOL, and SCAPS [38,39]. Among them, SCAPS presents unique advantages, such as the ability to simulate up to seven different layers with non-routine measurements (C-V, C-f). It can calculate many parameters such as spectral response, energy bands, ac characteristics, $J-V$ curve, and defect density, by just solving three basic semiconductor equations. It is user friendly and may be executed in both dark and light atmospheres [40–42]. Several studies confirm the good agreement of the simulation results with the experimental data, indicating the reliability of SCPAS software [43,44].

This work focuses on engineering the interface ETL/perovskite absorber layer. Optimizing the interfaces in the PCSs is essential for enhancing the photovoltaic performance. In this study, different materials were investigated as ETL, mainly TiO_2 and SnO_2. TiO_2 is the most common ETL for the fabrication of PSC [41]. On the other hand, SnO_2 has high electron mobility and keeps better band alignment with the $CsSnGeI_3$ absorber layer, which is supportive for electron extraction [45,46]. Cuprous oxide Cu_2O was used as the hole transport layer (HTL) due to its low cost, and it is widely used in solar energy materials, as a promising inorganic HTL for PSC applications [47]. The impact of the defect density and the thickness of the absorber layer on the overall performance of the proposed device was studied. For the first time, we show that an optimum $CsSnGeI_3$ device can have a simulated power conversion efficiency *PCE* of 30%.

2. Materials and Methods

In this numerical modeling, a comprehensive study has been performed on $CsSnGeI_3$, as the light harvesting material using SCAPS, which is 1D solar cell simulation software [47]. The software is specially designed to simulate multilayer solar cells, up to seven layers. SCAPS permits the calculation and observation of many electrical characteristics and parameters including current-density ($J - V$) curve, hetero-junction energy band structure, quantum efficiency (*QE*), open circuit voltage V_{oc}, short circuit J_{sc}, current density, power conversion efficiency (*PCE*), fill factor (*FF*), etc. The algorithm of SCPAS software is developed to solve the Poisson equation (Equation (1)) and the continuity equation of both charge carriers, electron (Equation (2)), and hole (Equation (3)).

$$\frac{d}{dx}\left(-\varepsilon(x)\frac{d\psi}{dx}\right) = q\left[p(x) - n(x) + N_D^+(x) - N_A^-(x) + p_t(x) - n_t(x)\right] \tag{1}$$

$$\frac{dp_n}{dt} = G_p - \frac{p_n - p_{n0}}{\tau_p} + p_n\mu_p\frac{d\xi}{dx} + \mu_p\xi\frac{dp_n}{dx} + D_p\frac{d^2 p_n}{dx^2} \tag{2}$$

$$\frac{dn_p}{dt} = G_n - \frac{n_p - n_{p0}}{\tau_n} + n_p\mu_n\frac{d\xi}{dx} + \mu_n\xi\frac{dn_p}{dx} + D_n\frac{d^2 n_p}{dx^2} \tag{3}$$

The device simulation is carried out in the $n-i-p$ configuration of FTO/ETL/CsSnGeI$_3$/ Cu$_2$O/Au, which is represented in Figure 1b. It was performed at 300 K under a standard illumination of 1000 W/m^2 and an air mass of AM 1.5G. The absorber layer is sandwiched between the HTL and ETL layers. Fluorine-doped tin oxide (FTO) is used as a front contact and gold (Au) as back metal contact. HTM Cu$_2$O is used for every structure, while five different ETLs are alternately used, and their performances are compared. The ETL includes: SnO$_2$, ZnO, IGZO, CdS, and TiO$_2$. Figure 1a shows the energy level diagram of the corresponding materials utilized in the device structure.
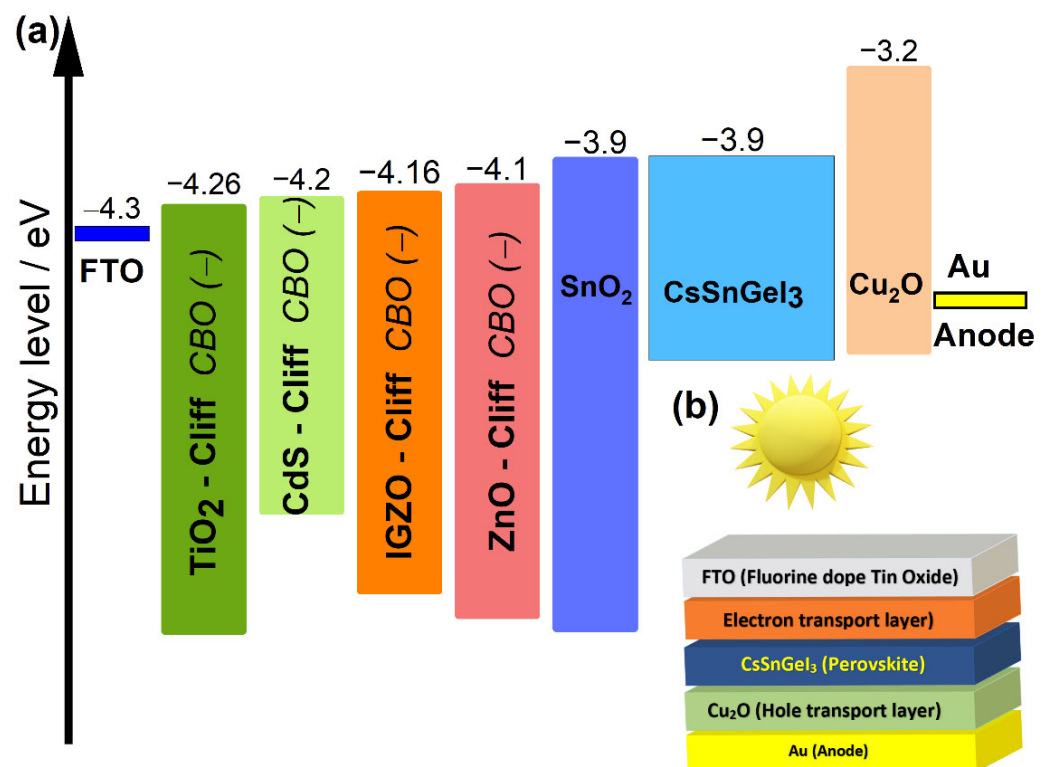

Figure 1. (**a**) Band alignment between ETL materials and CsSnGeI$_3$ perovskite. (**b**) Schematic diagram of lead-free CsSnGeI$_3$-based PSC structure.

Tables 1–3 show the list of values extracted from theories, experiments, and the literature [48–57]. The parameters have been considered, while forming a base configuration to start with the simulation process. Different properties, such as the thickness and defect density of the absorber layer, have been varied to obtain an optimized result and to study their impacts on the device performance. Initially, the thickness of FTO (400 nm), ETL (50 nm), and Cu$_2$O (350 nm) were optimized for high *PCE*, as mentioned in Table 1.

Table 1. Electrical and optical properties used in simulation of CsSnGeI$_3$-based perovskite solar cell.

Parameters	FTO [56]	SnO$_2$ (ETL) [54,55]	CsSnGeI$_3$ (Absorber) [36]	Cu$_2$O [48,50]
Thickness (μm)	0.4	0.05	1.5	0.350
Bandgap E_g(eV)	3.5	3.6	1.5	2.170
Electron Affinity χ(eV)	4.3	3.90	3.90	3.2
Dielectric permittivity	9	8	28	7.11
CB effective density of states (cm^{-3})	2.2×10^{18}	3.16×10^{18}	3.1×10^{18}	2×10^{17}
VB effective density of states (cm^{-3})	1.8×10^{19}	2.5×10^{19}	3.1×10^{18}	1.1×10^{19}
Electron mobility $(\text{cm}^2/\text{V} \cdot \text{s})$	20	15	974	20
Hole mobility $(\text{cm}^2/\text{V} \cdot \text{s})$	10	0.1	213	80
Donor Concentration $N_D(\text{cm}^{-3})$	1×10^{18}	1×10^{17}	0	1×10^7
Acceptor concentration $N_A(\text{cm}^{-3})$	0	0	1×10^{19}	1×10^{18}

Table 2. Electrical and optical properties of different ETL materials.

Parameters	ZnO [51,52]	IGZO [51,52]	CdS [53,57]	TiO$_2$ [49]
Thickness (μm)	0.05	0.05	0.05	0.05
Bandgap E_g(eV)	3.3	3.05	2.4	3.260
Electron Affinity χ(eV)	4.1	4.160	4.2	4.26
Dielectric permittivity	9	10	10	32
CB effective density of states (cm^{-3})	1×10^{19}	5×10^{18}	2.2×10^{18}	1×10^{19}
VB effective density of states (cm^{-3})	1×10^{19}	5×10^{18}	1×10^{19}	1×10^{19}
Electron mobility $(\text{cm}^2/\text{V} \cdot \text{s})$	50	15	100	20
Hole mobility $(\text{cm}^2/\text{V} \cdot \text{s})$	5	0.1	25	10
Donor Concentration $N_D(\text{cm}^{-3})$	1×10^{17}	1×10^{17}	2×10^{18}	1×10^{17}
Acceptor concentration $N_A(\text{cm}^{-3})$	0	0	0	0

Table 3. Defect density values inside the layers and at interface of the device.

Parameters	ETL	HTL	CsSnGeI$_3$	HTL/CsSnGeI$_3$	CsSnGeI3/ETL
Defect Type	Neutral	Neutral	Neutral	Neutral	Neutral
Capture cross section for electrons $\sigma_n(\text{cm}^{-2})$	1×10^{-15}	1×10^{-15}	1×10^{-15}	1×10^{-18}	1×10^{-15}
Capture cross section for hole $\sigma_p(\text{cm}^{-2})$	1×10^{-15}	1×10^{-15}	1×10^{-15}	1×10^{-16}	1×10^{-15}
Energetic distribution	Single	Single	Gaussian	Single	Single
Energy level with respect to E_v (above E_v) (eV)	0.6	0.650	0.6	0.6	0.6
Characteristic energy (eV)	0.1	0.1	0.1	0.1	0.1
Total density $N_t(\text{cm}^{-3})$	1×10^{15}	1×10^{14}	1×10^{15}	1×10^{12}	1×10^{11}

3. Results and Discussions

3.1. Effect of ETLs on Solar Cell Performance

The $n - i - p$ PSC structures for three different ETL are analyzed for the same absorber (CsSnGeI$_3$) layer thickness, 1.5 μm, and the same absorber bulk defect densities,

1×10^{15} cm^{-3}. It should be mentioned that these values are selected and fixed after optimizing the device performance. The thickness and the defect concentration of the perovskite layer were investigated and varied, until the optimal performance of the solar cell is found. The $J - V$ characteristics for the five structures are shown in Figure 2a, while the open circuit voltage (V_{oc}), performance cell efficiency (PCE), and fill factor (FF) are plotted, respectively, in Figure 2b–d. Figure 2b reveals that the five simulated cells exhibit the same current level of 28 mA·cm^{-2}.
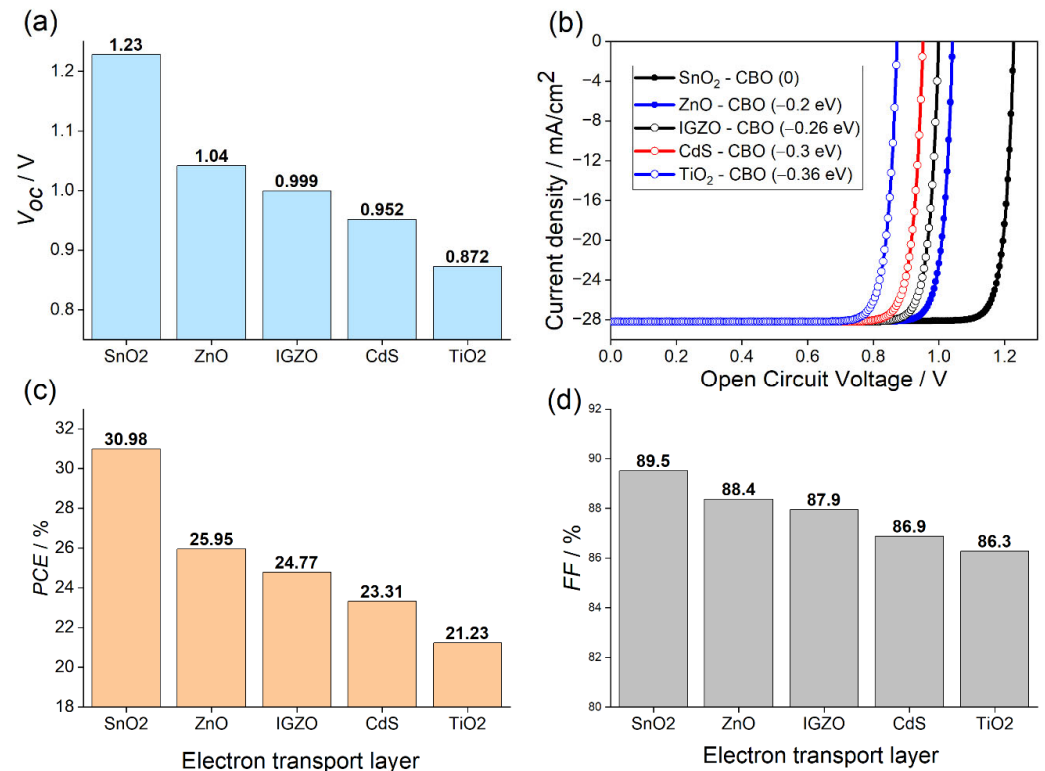
Figure 2. Variation in (**a**) V_{oc}, (**b**) $J - V$ characteristics, (**c**) PCE, and (**d**) FF for different ETL materials simulated in PSC.

Surprisingly, all ETLs had superior performance over TiO$_2$, the most commonly used ETL in perovskite studies due to its mesoscopic structure. It is observed that the PSC with SnO$_2$ acquired the highest PCE of 30.9% and V_{oc} of 1.22 V. The most credible reason of this behavior is the excellent band alignment with the CsSnGeI$_3$ layer shown in Figure 1a, where there is no conduction band offset (CBO) ($\Delta E_c = 0$) at the SnO$_2$/CsSnGeI$_3$ interface. In fact, CBO is the energy difference ΔE_c between the CB level of ETL and that of the perovskite. When the CB level of ETL is lower than that of the perovskite, ΔE_c will be negative and an energy cliff will be formed at the ETL/perovskite interface. An energy cliff structure does not hinder the photo-generated electron flow, but it may cause the interfacial recombination to occupy the main position of recombination of the PSC device [58,59]. When the energy cliff is formed, there is no potential barrier for electrons at the ETL/perovskite interface. The energy barrier that the electron transport must overcome from the conduction band of the ETL to the interface ETL/perovskite is $\Delta E_c + qV_D$, here q is the charge of the carrier and V_D is the built-in potential. Since ΔE_c is negative for all devices, except the one with SnO$_2$ ETL, the electrons in the ETL layer can easily cross the barrier to attain the interface. The cliff formation can improve the accumulation near to ETL/perovskite, which in turn enhances the recombination in this area by back-transfer to the interface of heterojunction.

Under open-circuit conditions, the interfacial recombination mainly occurs through the pathways of back-transfer recombination, where the electrons that have been injected into the FTO electrode, and the free holes in the absorber recombine through the deep level defect at the ETL/absorber interface, which then result in a serious V_{oc} deficit. Then, the

PCE drops, which has been confirmed by our results plotted in Figure 2a,c. They exhibit that the V_{oc} as well as the *PCE* dramatically decrease with the increase in the absolute value of ΔE_c. It was observed in Figure 2d that *FF* is improved with devices having a larger V_{oc}. The solar cell with the benchmark material TiO_2 ETL yields the lowest *PCE* of 21.23%, V_{oc} of 0.872 V, and *FF* of 86.3%, owing this to the largest CBO among all the tested materials ($\Delta E_c = -0.36$ eV), comparable to the best performance obtained in recent studies on similar perovskite [60].

Finally, it can be concluded that the band alignment plays one of the key roles for having higher *PCE*, V_{oc}, and *FF*. Thus, SnO_2 is finally selected as the optimal ETL material for the proposed lead-free PSC.

3.2. Effect of Absorber Layer Defects Density N_t

Although the interface engineering and the control at the ETL/perovskite interface is crucial for achieving a high-efficiency solar cell device, the morphology and quality of the light absorber film have been recently recognized as a major factor for determining PSC performance [61], given that the photoelectrons are mainly generated in this layer. Thus, to further enhance the PSC performance with SnO_2 ETL and to determine the influence of absorber defect density on cell performance, the defect density of the perovskite layer has been considered. The defect density values simulated in this study range from $10^{14} cm^{-3}$ to 10^{19} cm^{-3}, based on values from previous studies on lead [62,63]. As shown in Figure 3a–d, when the defect density is below $N_t = 10^{16}$ cm^{-3}, the photovoltaic response of the cell remains almost unchanged, except V_{oc}, which starts to decrease. The PSC performance properties start to deteriorate when the defect density exceeds 10^{16} cm^{-3}, until reaching their lowest performance values of $V_{oc} = 1.06$ V, $J_{sc} = 11.79$ mA $\cdot$ cm^{-2}, *PCE* = 9.61%, and *FF* = 76.46%.
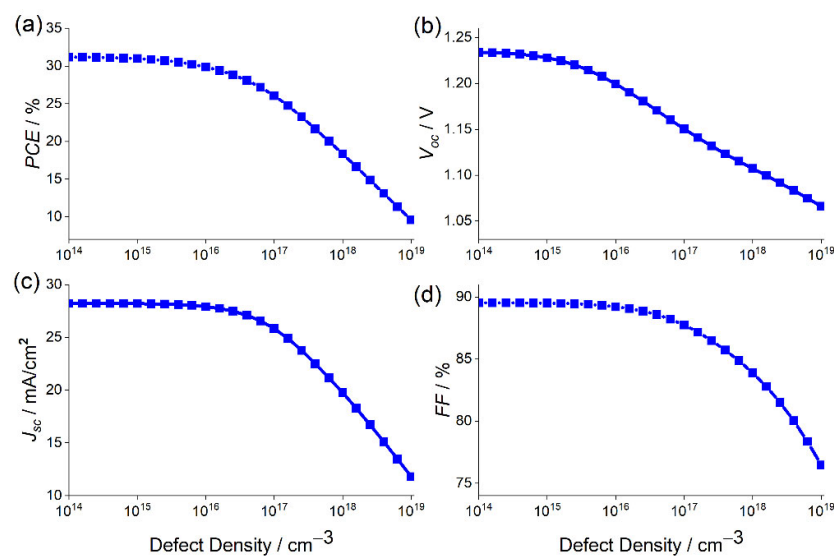

Figure 3. Photovoltaic characteristics of (**a**) *PCE*, (**b**) V_{oc}, (**c**) J_{sc} and (**d**) *FF* as a function of the defect density of the absorber layer.

The perovskite defect density effect can be explained by the Shockley–Read–Hall (SRH) recombination model [64,65]. In this work, to clearly understand the defect density effect of the absorber on the performance of the device, the variation of the SRH recombination rate with depth from the surface for different values of defect density was studied and depicted in Figure 4. It is detected that the recombination rate increases with the increase in the defect density. Consequently, V_{oc} and *PCE* decrease, as shown in Figure 3a,b. It can be observed that the recombination rate not only increases in the absorber layer between 350 nm and 1850 nm but also at the perovskite/ETL interface, reaching a maximum of 7×10^{21} cm$^{-3} \cdot$ s^{-1}.
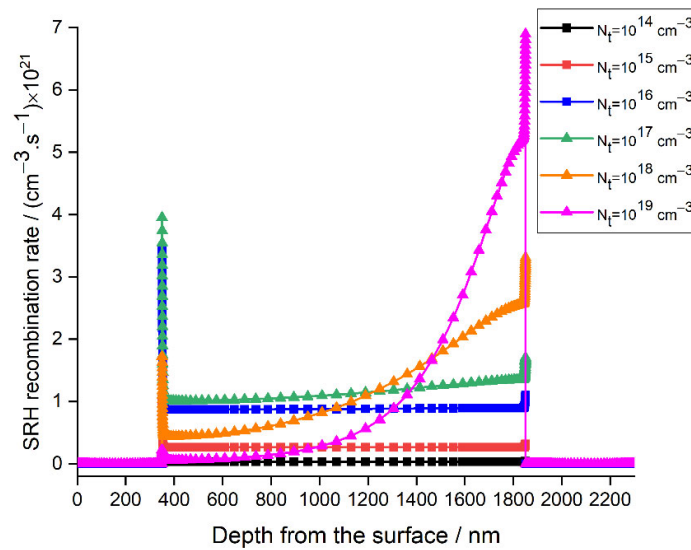
Figure 4. Effect of the absorber layer defect density on the recombination rate with depth from the surface.

According to the SRH model, the recombination rate can be expressed by:

$$R^{SRH} = \frac{\tau_{n,p}^{-1}\left(n \cdot p - n_i^2\right)}{n + p + 2n_i coh\left(\frac{E_t - E_i}{KT}\right)} \tag{4}$$

where, $\tau_{n,p}, n, p, n_i, E_i,$ and E_t represent the lifetime of charge carriers, electron density, hole density, intrinsic density, intrinsic energy level, and energy level of the trap defects, respectively.

The lifetime of charge carriers $(\tau_{n,p})$, the diffusion coefficient (D), and the diffusion length of charge carrier (L_D) are represented in the following equations:

$$\tau_{n,p} = \frac{1}{\sigma_{n,p} v_{th} N_t} \tag{5}$$

$$L_D = \sqrt{D\tau} \tag{6}$$

$$D = \frac{\mu \cdot K_B T}{q} \tag{7}$$

where μ is the mobility of charge carriers, T is the temperature in Kelvin, K_B is the Boltzmann constant, and q the magnitude of the charge.

It can be deduced from Equations (4)–(7) that as the defect density in the perovskite layer increases, the carrier lifetime decreases, while the charge recombination will increase, as confirmed in Figure 4, leading to a drop in V_{oc} and J_{sc}. Moreover, when the doping density is comparable or lower than that of the defect density in the absorber, the device becomes semi-insulating and the desired p-n junction will not be formed [66], resulting in inferior cell performance. This scenario was confirmed by the current study, wherein the doping density for CsSnGeI$_3$ is 10^{17} cm^{-3}, and the performance of the device starts to worsen when the defect density exceeds 10^{16} cm^{-3}.

It can be observed from Equation (7) that the diffusion coefficient is proportional to the mobility of charge carrier, the electron mobility (974 cm^2/V · s), and hole mobility (213 cm^2/V · s), being larger for CsSnGeI$_3$. Due to the large value of mobility, the diffusion length is high, and that is why our simulated PSC shows a high efficiency of 30.98% with $N_t = 10^{15}$ cm^{-3}. Thus, to achieve optimum PSC performance, the defect density in the absorber layer has to be significantly reduced. Experimental studies have proven that the fabrication of the tin-based perovskite device, with defect density as low as $N_t = 10^{15}$ cm^{-3}, is completely feasible [67], so we set this defect density as an optimized value. By fixing

$N_t = 10^{15} \text{cm}^{-3}$, the cell performance reaches its maximum performance, attaining a J_{sc} of 28.19 mA · cm^{-2}, *PCE* of 30.98%, *FF* of 89.52%, and V_{oc} of 1.22 V. Further decreasing the defect density from $N_t = 10^{15}$ cm^{-3} to $N_t = 10^{14}$ cm^{-3} has a negligible effect. The obtained performance is found to be largely better than the previously published results for lead-free perovskite solar cells [60].

3.3. Influence of the Absorber Layer Thickness

The thickness of the light-absorbing layer plays a crucial role in optimizing the solar cell performance. It should be chosen as high to maximize the current density, but not too much, as it minimizes the reverse saturation current. The influence of the absorber layer thickness on the device photovoltaic outputs has been studied, by varying it from 0.1 μm to 2 μm while maintaining all the other parameters as given in Table 1. Figure 5a–d depicts the PSC performance statistics, including V_{oc}, J_{sc}, *PCE*, and *FF*. It can be observed that the effect of absorber layer thickness is minimal. A *FF* of 89.16% and 89.50% are obtained at an absorber layer thickness of 0.1 μm and 0.6 μm, respectively, then it saturates. The value of V_{oc} is obtained to be 1.214 V at 0.1 μm and increases up to a maximum of 1.230 V at 0.6 μm, then it decreases to 1.225 V at 0.6 μm. The decreases in V_{oc} with thickness is attributed to the increase in the dark saturation current, which increases the recombination of the charge carrier. This dependency of the dark saturation current J_0, V_{oc}, and J_{sc}, is given by [68]:

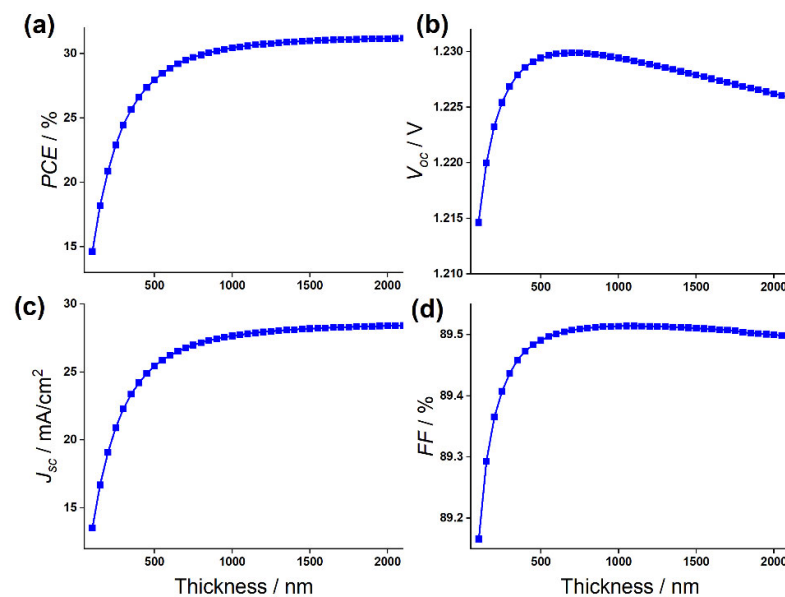$$V_{oc} = \frac{K_B T}{q} Ln\left[\frac{J_{sc}}{J_0} + 1\right] \tag{8}$$

Figure 5. Change in (**a**) *PCE*, (**b**) V_{oc}, (**c**) J_{sc}, and (**d**) *FF* against the CsSnGeI$_3$ absorber layer thickness variation.

It is seen in Figure 5c that J_{sc} increases linearly, up to an absorber thickness of 1 μm, then it almost saturates with an increasing absorber thickness. The J_{sc} of 13.51 mA · cm^{-2} and 28.45 mA · cm^{-2} are estimated for a thickness of 0.1 and 2 μm, respectively. The great enhancement of J_{sc}, with an increase in the absorber thickness, is attributed to the generation of more electron-hole pairs in the perovskite, leading to an efficiency enhancement. The trend of *PCE* as a function of CsSnGeI$_3$ was strongly correlated with the trend of J_{sc}, and *PCE*s of 14.63% and 31% are estimated for a thickness of 0.1 and 2 μm, respectively.

Figure 6 depicts quantum efficiency vs. wavelength for various absorber thicknesses ranging from 0.1 μm. to 1 μm. Quantum efficiency indicates to what extent a solar cell can collect carriers from incident photons of a given energy. It can be observed that the decrease

in absorber thickness leads to reduced photon absorption at a longer wavelength. This is due to fewer photogenerated electron-hole pairs inside the absorber layer. In addition, at wavelengths larger than 830 nm, quantum efficiency falls to zero as light is not absorbed below the bandgaps, at longer, low energy wavelengths. A loss of quantum efficiency can be observed for wavelengths below 350 nm for all simulated solar cells. This is because the light is mainly absorbed by the FTO substrate and SnO_2 layer.
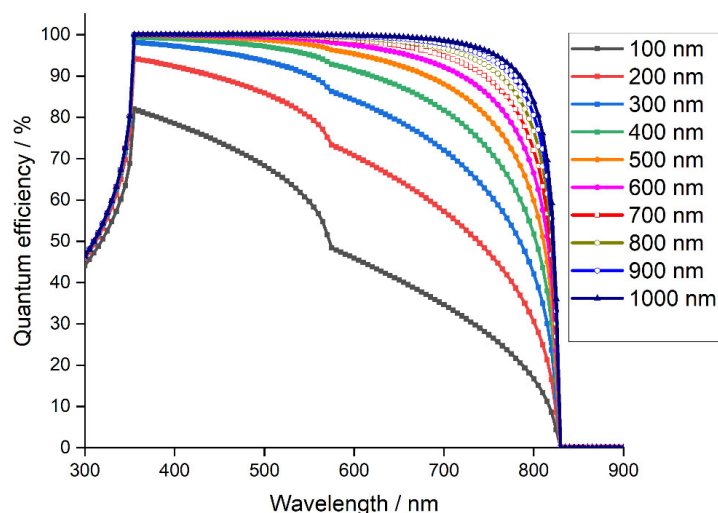

Figure 6. Quantum efficiency of the simulated device with absorber layer thickness.

The larger *QE* is reached with an absorber thickness of 1 μm. Ultimately, the best performing device has a perovskite layer 1.5 μm thick with J_{sc} of 28.19 mA · cm^{-2}, *PCE* of 30.98%, *FF* of 89.52%, and V_{oc} of 1.22 V.

4. Conclusions

In this work, a novel lead-free $CsSnGeI_3$-based perovskite solar cell has been thoroughly investigated. A normal n-i-p planar structure of FTO/ETL/CsSnGeI3/Cu2O/Au is numerically simulated and analyzed using SCAPS-1D simulation software. The impact of various ETL on the device performance was studied to get the highest possible efficiency. It has been demonstrated that a PSC with SnO_2 ETL has, by far, the best performance, owing to its excellent band alignment with the perovskite layer. Furthermore, the photovoltaic performance of the cell has been optimized by tuning two major factors: $CsSnGeI_3$ defect density and absorber layer thickness. Our study explained the significant effect of these two factors on the electrical parameters of the PSC. The results revealed that the optimal light absorber thickness and the optimal absorber defect density were 1.5 μm and 10^{15} cm^{-3}, respectively. Reducing the absorber defect density significantly enhances the *PCE* to reach an unprecedented result of almost 31%. Thus, future research should focus on refining the device fabrication techniques. Our novel results could provide a viable path to fabricate cost-effective, highly efficient, and stable $CsSnGeI_3$-based perovskite solar cells.

References

1. Grätzel, M. The light and shade of perovskite solar cells. *Nat. Mater.* **2014**, *13*, 838–842. [CrossRef] [PubMed]
2. Bhattacharya, S.; John, S. Beyond 30% Conversion Efficiency in Silicon Solar Cells: A Numerical Demonstration. *Sci. Rep.* **2019**, *9*, 12482. [CrossRef] [PubMed]
3. Tawalbeh, M.; Al-Othman, A.; Kafiah, F.; Abdelsalam, E.; Almomani, F.; Alkasrawi, M. Environmental impacts of solar photovoltaic systems: A critical review of recent progress and future outlook. *Sci. Total Environ.* **2021**, *759*, 143528. [CrossRef] [PubMed]
4. Green, M.A. Tracking solar cell conversion efficiency. *Nat. Rev. Phys.* **2020**, *2*, 172–173. [CrossRef]
5. Kour, R.; Arya, S.; Verma, S.; Gupta, J.; Bandhoria, P.; Bharti, V.; Datt, R.; Gupta, V. Potential Substitutes for Replacement of Lead in Perovskite Solar Cells: A Review. *Glob. Chall.* **2019**, *3*, 1900050. [CrossRef] [PubMed]
6. Shockley, W.; Queisser, H.J. Detailed balance limit of efficiency of p-n junction solar cells. *J. Appl. Phys.* **1961**, *32*, 510. [CrossRef]
7. Yoshikawa, K.; Kawasaki, H.; Yoshida, W.; Irie, T.; Konishi, K.; Nakano, K.; Uto, T.; Adachi, D.; Kanematsu, M.; Uzu, H.; et al. Silicon Heterojunction solar cell with interdigitated back contacts for a photoconversion efficiency over 26%. *Nat. Energy* **2017**, *2*, 17032. [CrossRef]
8. Levi, D.H.; Green, M.A.; Hishikawa, Y.; Dunlop, E.D.; Hohl-Ebinger, J.; Ho-Baillie, A.W. Solar cell efficiency tables (version 51). *Prog. Photovolt. Res. Appl.* **2018**, *26*, 3.
9. Parida, B.; Iniyan, S.; Goic, R. A review of solar photovoltaic technologies. *Sustain. Energy Rev.* **2011**, *15*, 1625. [CrossRef]
10. Saive, R. Light trapping in thin silicon solar cells: A review on fundamentals and technologies. *Prog. Photovolt. Res. Appl.* **2021**, *29*, 1125–1137. [CrossRef]
11. Huang, H.H.; Shih, Y.C.; Wang, L.; Lin, K.F. Boosting the ultra-stable unencapsulated perovskite solar cells by using montmorillonite/ CH3NH3PbI3 nanocomposite as photoactive layer. *Energy Environ. Sci.* **2019**, *12*, 1265–1273. [CrossRef]
12. Yang, W.S.; Park, B.-W.; Jung, E.H.; Jeon, N.J.; Kim, Y.C.; Lee, D.U.; Shin, S.S.; Seo, J.; Kim, E.K.; Noh, J.H.; et al. Iodide management in formamidinium-lead-halide-based perovskite layers for efficient solar cells. *Science* **2017**, *356*, 1376–1379. [CrossRef] [PubMed]
13. Shih, Y.-C.; Lan, Y.-B.; Li, C.-S.; Hsieh, H.-C.; Wang, L.; Wu, C.-I.; Lin, K.-F. Amino-acid-induced preferential orientation of perovskite crystals for enhancing interfacial charge transfer and photovoltaic performance. *Small* **2017**, *13*, 1604305–1604314. [CrossRef] [PubMed]
14. Eperon, G.E.; Burlakov, V.M.; Docampo, P.; Goriely, A.; Snaith, H.J. Morphological Control for High Performance, Solution-Processed Planar Heterojunction Perovskite Solar Cells. *Adv. Funct. Mater.* **2014**, *24*, 151–157. [CrossRef]
15. Liu, M.; Johnston, M.B.; Snaith, H.J. Efficient planar heterojunction perovskite solar cells by vapour deposition. *Nat. Cell Biol.* **2013**, *501*, 395–398. [CrossRef]
16. Kim, H.S.; Im, S.H.; Park, N.G. Organolead halide perovskite: New horizons in solar cell research. *J. Phys. Chem. C* **2014**, *118*, 5615–5625. [CrossRef]
17. Gao, F.; Li, C.; Qin, L.; Zhu, L.; Huang, X.; Liu, H.; Liang, L.; Hou, Y.; Lou, Z.; Hu, Y.; et al. Enhanced performance of tin halide perovskite solar cell by addition of lead thiocyanate. *RSC Adv.* **2018**, *8*, 14025–14030. [CrossRef]
18. Wang, X.; Zhang, T.; Lou, Y.; Zhao, Y. All-inorganic lead-free perovskites for optoelectronic applications. *Mater. Chem. Front.* **2019**, *3*, 365. [CrossRef]
19. Miyata, A.; Mitioglu, A.; Plochocka, P.; Portugall, O.; Wang, J.T.-W.; Stranks, S.D.; Snaith, H.; Nicholas, R. Direct measurement of the exciton binding energy and effective masses for charge carriers in organic–inorganic tri-halide perovskites. *Nat. Phys.* **2015**, *11*, 582–587. [CrossRef]
20. Huang, J.; Yuan, Y.; Shao, Y.; Yan, Y. Understanding the physical properties of hybrid perovskites for photovoltaic applications. *Nat. Rev. Mater.* **2017**, *2*, 17042. [CrossRef]
21. Jeon, N.J.; Na, H.; Jung, E.H.; Yang, T.-Y.; Lee, Y.G.; Kim, G.; Shin, H.-W.; Seok, S.I.; Lee, J.; Seo, J. A fluorene-terminated hole-transporting material for highly efficient and stable perovskite solar cells. *Nat. Energy* **2018**, *3*, 682–689. [CrossRef]
22. Hao, F.; Stoumpos, C.C.; Chang, R.P.H.; Kanatzidis, M.G. Anomalous Band Gap Behavior in Mixed Sn and Pb Perovskites Enables Broadening of Absorption Spectrum in Solar Cells. *J. Am. Chem. Soc.* **2014**, *136*, 8094. [CrossRef] [PubMed]
23. Chen, J.; Zhou, S.; Jin, S.; Li, H.; Zhai, T. Crystal organometal halide perovskites with promising optoelectronic applications. *J. Mater. Chem. C* **2016**, *4*, 11. [CrossRef]
24. Shen, Q.; Ogomi, Y.; Chang, J.; Toyoda, T.; Fujiwara, K.; Yoshino, K.; Sato, K.; Yamazaki, K.; Akimoto, M.; Kuga, Y.; et al. Optical absorption, charge separation and recombination dynamics in Sn/Pb cocktail perovskite solar cells and their relationships to photovoltaic performances. *J. Mater. Chem. A* **2015**, *3*, 9308. [CrossRef]
25. Wang, Y.; Muryobayashi, T.; Nakada, K.; Li, Z.; Yamada, A. Correlation between carrier recombination and valence band offset effect of graded Cu(In,Ga)Se$_2$ solar cells. *Sol. Energy Mater. Sol. Cells* **2019**, *201*, 110070. [CrossRef]
26. Dang, Y.; Zhou, Y.; Liu, X.; Ju, D.; Xia, S.; Xia, H.; Tao, X. Formation of hybrid perovskite tin iodide single crystals by topseeded solution growth. *Angew. Chem. Int. Ed.* **2016**, *55*, 3447–3450. [CrossRef]
27. Zhou, Y.; Zhou, Z.; Chen, M.; Zong, Y.; Huang, J.; Pang, S.; Padture, N.P. Doping and alloying for improved perovskite solar cells. *J. Mater. Chem. A* **2016**, *4*, 17623–17635. [CrossRef]
28. Yu, C.; Chen, Z.; Wang, J.J.; Pfenninger, W.; Vockic, N.; Kenney, J.T.; Shum, K. Temperature dependence of the band gap of perovskite semiconductor compound CsSnI$_3$. *J. Appl. Phys.* **2011**, *110*, 063526. [CrossRef]

29. Chung, I.; Lee, B.; He, J.; Chang, R.P.H.; Kanatzidis, M.G. All-solid-state dye-sensitized solar cells with high efficiency. *Nature* **2012**, *485*, 486–489. [CrossRef]

30. Chen, Z.; Yu, C.; Shum, K.; Wang, J.J.; Pfenninger, W.; Vockic, N.; Midgley, J.; Kenney, J.T. Photoluminescence study of polycrystalline CsSnI3 thin films: Determination of exciton binding energy. *J. Lumin.* **2012**, *132*, 345–349. [CrossRef]

31. Xie, F.; Zhou, S.; Zhao, N.; Hui, H. Native defect-induced hysteresis behavior in organolead iodide perovskite solar cells. *Adv. Func. Mater.* **2016**, *26*, 1411–1419.

32. Wang, N.; Zhou, Y.; Ju, M.G.; Garces, H.F.; Ding, T.; Pang, S.; Zeng, X.C.; Padture, N.P.; Sun, X.W. Heterojunction-depleted lead-free perovskite solar cells with coarse-grained B-γ-CsSnI$_3$ thin films. *Adv. Energy Mater.* **2016**, *6*, 1670137.

33. Marshall, K.P.; Walker, M.; Walton, R.I.; Hatton, R.A. Enhanced stability and efficiency in hole-transport-layer-free CsSnI$_3$ perovskite photovoltaics. *Nat. Energy* **2016**, *1*, 16178. [CrossRef]

34. Li, B.; Di, H.; Chang, B.; Yin, R.; Fu, L.; Zhang, Y.; Yin, L. Efficient passivation strategy on Sn related defects for high performance all-inorganic CsSnI3 perovskite solar cells. *Adv. Funct. Mater.* **2021**, *31*, 2007447. [CrossRef]

35. Ye, T.; Wang, X.; Wang, K.; Ma, S.; Yang, D.; Hou, Y.; Yoon, J.; Wang, K.; Priya, S. Localized electron density engineering for stabilized B-γ CsSnI$_3$-based perovskite solar cells with efficiencies >10%. *ACS Energy Lett.* **2021**, *6*, 1480–1489. [CrossRef]

36. Chen, M.; Ju, M.G.; Garces, H.F.; Carl, A.D.; Ono, L.K.; Hawash, Z.; Zhang, Y.; Shen, T.; Qi, Y.; Grimm, R.L.; et al. Highly stable and efficient all-inorganic lead-free perovskite solar cells with native-oxide passivation. *Nat. Commun.* **2019**, *10*, 16. [CrossRef] [PubMed]

37. Burgelman, M.; Nollet, P.; Degrave, S. Modelling polycrystalline semiconductor solar cells. *Thin Solid Film.* **2000**, *361*, 527–532. [CrossRef]

38. Feng, L.; Zhu, J.; Wei, J.; Li, Y.; Lv, M.; Yang, S.; Zhang, B.; Yao, J.; Dai, S. Numerical simulation: Toward the design of high-efficiency planar perovskite solar cells. *Appl. Phys. Lett.* **2014**, *104*, 253508.

39. Zandi, S.; Saxena, P.; Gorji, N. Numerical simulation of heat distribution in RGO-contacted perovskite solar cells using COMSOL. *Sol. Energy* **2020**, *197*, 105–110. [CrossRef]

40. Huang, L.; Sun, X.; Li, C.; Xu, R.; Xu, J.; Du, Y.; Wu, Y.; Ni, J.; Cai, H.; Li, J.; et al. Electron transport layer-free planar perovskite solar cells: Further performance enhancement perspective from device simulation. *Sol. Energy Mater. Sol. Cells* **2016**, *157*, 1038–1047. [CrossRef]

41. Mouchou, R.T.; Jen, T.C.; Laseinde, O.T.; Ukoba, K.O. Numerical simulation and optimization of p-NiO/n-TiO$_2$ solar cell system using SCAPS. *Mater. Today Proc.* **2021**, *38*, 835–841. [CrossRef]

42. Decock, K.; Khelifi, S.; Burgelman, M. Modelling multivalent defects in thin film solar cells. *Thin Solid Film.* **2011**, *519*, 7481–7484. [CrossRef]

43. Minbashi, M.; Omrani, M.K.; Memarian, N.; Kim, D.H. Comparison of theoretical and experimental results for band-gap-graded CZTSSe solar cell. *Curr. Appl. Phys.* **2017**, *17*, 1238–1243. [CrossRef]

44. Karthick, S.; Velumani, S.; Bouclé, J. Experimental and SCAPS simulated formamidinium perovskite solar cells: A comparison of device performance. *Sol. Energy* **2020**, *205*, 349–357. [CrossRef]

45. Tavakoli, M.; Tavakoli, R.; Hasanzadeh, S.; Mirfasih, M. Interface Engineering of Perovskite Solar Cell Using a Reduced-Graphene Scaffold. *J. Phys. Chem. C* **2016**, *12*, 19531–19536. [CrossRef]

46. Tavakoli, M.; Giordano, F.; Zakeeruddin, S.; Grätzel, M. Mesoscopic Oxide Double Layer as Electron Specific Contact for Highly Efficient and UV Stable Perovskite Photovoltaics. *Nano Lett.* **2018**, *18*, 2428–2434. [CrossRef]

47. Chatterjee, S.; Pal, A.J. Introducing Cu2O thin films as a hole-transport layer in efficient planar perovskite solar cell structures. *J. Phys. Chem. C* **2016**, *120*, 1428–1437. [CrossRef]

48. Shasti, M.; Mortezaali, A. Numerical Study of Cu$_2$O, SrCu$_2$O$_2$, and CuAlO$_2$ as Hole-Transport Materials for Application in Perovskite Solar Cells. *Phys. Status Solidi A* **2019**, *216*, 1900337. [CrossRef]

49. Hao, F.; Stoumpos, C.C.; Cao, D.H.; Chang, R.P.H.; Kanatzidis, M.G. Lead-free solid-state organic–inorganic halide perovskite solar cells. *Nat. Photon.* **2014**, *8*, 489–494. [CrossRef]

50. Patel, P.K. Device simulation of highly efficient eco-friendly CH$_3$NH$_3$SnI$_3$ perovskite solar cell. *Sci. Rep.* **2021**, *11*, 3082. [CrossRef]

51. Lakhdar, N.; Hima, A. Electron transport material effect on performance of perovskite solar cells based on CH$_3$NH$_3$GeI$_3$. *Opt. Mater.* **2020**, *99*, 109517. [CrossRef]

52. Azri, F.; Meftah, A.; Sengouga, N.; Meftah, A. Electron and hole transport layers optimization by numerical simulation of a perovskite solar cell. *Sol. Energy* **2019**, *181*, 372–378. [CrossRef]

53. Guo, Y.; Jiang, J.; Zuo, S.; Shi, F.; Tao, J.; Hu, Z.; Hu, X.; Hu, G.; Yang, P.; Chu, J. RF sputtered CdS films as independent or buffered electron transport layer for efficient planar perovskite solar cell. *Sol. Energy Mater. Sol. Cells* **2018**, *178*, 186–192. [CrossRef]

54. Rahman, M.S.; Miah, S.; Marma, M.S.W.; Sabrina, T. Simulation based Investigation of Inverted Planar Perovskite Solar Cell with All Metal Oxide Inorganic Transport Layers. In Proceedings of the International Conference on Electrical, Computer and Communication Engineering (ECCE), Cox's Bazar, Bangladesh, 7–9 February 2019; pp. 1–6.

55. Baena, J.P.C.; Steier, L.; Tress, W.; Saliba, M.; Neutzner, S.; Matsui, T.; Giordano, F.; Jacobsson, T.J.; Kandada, A.R.S.; Zakeeruddin, S.M.; et al. Highly efficient planar perovskite solar cells through band alignment engineering. *Energy Environ. Sci.* **2015**, *8*, 2928–2934. [CrossRef]

56. Noh, M.F.M.; Teh, C.H.; Daik, R.; Lim, E.L.; Yap, C.C.; Ibrahim, M.A.; Ludin, N.A.; Yusoff, A.R.B.M.; Jang, J.; Teridi, M.A.M. The architecture of the electron transport layer for a perovskite solar cell. *J. Mater. Chem. C* **2018**, *6*, 682–712.

57. Hao, L.; Li, T.; Ma, X.; Wu, J.; Qiao, L.; Wu, X.; Hou, G.; Pei, H.; Wang, X.; Zhang, X. A tin-based perovskite solar cell with an inverted hole-free transport layer to achieve high energy conversion efficiency by SCAPS device simulation. *Opt. Quant. Electron.* **2021**, *53*, 524. [CrossRef]

58. Minemoto, T.; Hashimoto, Y.; Satoh, T.; Negami, T.; Takakura, H. Variable Light Soaking Effect of Cu(In,Ga)Se$_2$ Solar Cells with Conduction Band Offset Control of Window/Cu(In,Ga)Se$_2$ Layers. *MRS Online Proc. Libr.* **2007**, *1012*, 703. [CrossRef]

59. Liu, H.; Tang, J.; Kramer, I.J.; Debnath, R.; Koleilat, G.I.; Wang, X.; Fisher, A.; Li, R.; Brzozowski, L.; Levina, L.; et al. Electron acceptor materials engineering in colloidal quantum dot solar cells. *Adv. Mater.* **2011**, *33*, 3832–38327. [CrossRef]

60. Singh, N.; Agarwal, A.; Agarwal, M. Numerical simulation of highly efficient lead-free perovskite layers for the application of all-perovskite multi-junction solar cell. *Superlattices Microstruct.* **2021**, *149*, 106750. [CrossRef]

61. Xing, G.; Mathews, N.; Sun, S.; Lim, S.S.; Lam, Y.M.; Grätzel, M.; Mhaisalkar, S.; Sum, T.C. Long-Range Balanced Electron- and Hole-Transport Lengths in Organic-Inorganic CH$_3$NH$_3$PbI$_3$. *Science* **2013**, *342*, 344–347. [CrossRef]

62. Kemp, K.W.; Labelle, A.J.; Thon, S.M.; Ip, A.H.; Kramer, I.J.; Hoogland, S.; Sargent, E.H. Interface Recombination in Depleted Heterojunction Photovoltaics based on Colloidal Quantum Dots. *Adv. Energy Mater.* **2013**, *3*, 917–922. [CrossRef]

63. Minemoto, T.; Murata, M. Device modeling of perovskite solar cells based on structural similarity with thin film inorganic semiconductor solar cells. *J. Appl. Phys.* **2014**, *116*, 054505. [CrossRef]

64. Haider, S.Z.; Anwar, H.; Wang, M. A comprehensive device modelling of perovskite solar cell with inorganic copper iodide as hole transport material. *Semicond. Sci. Technol.* **2018**, *33*, 035001. [CrossRef]

65. Abdelaziz, S.; Zekry, A.; Shaker, A.; Abouelatta, M. Investigating the performance of formamidinium tin-based perovskite solar cell by SCAPS device simulation. *Opt. Mater.* **2020**, *101*, 109738. [CrossRef]

66. Devi, N.; Parrey, K.A.; Aziz, A.; Datta, S. Numerical simulations of perovskite thin-film solar cells using a CdS hole blocking layer. *J. Vac. Sci. Technol. B* **2018**, *36*, 04G105. [CrossRef]

67. Du, H.J.; Wang, W.C.; Zhu, J.Z. Device simulation of lead-free CH$_3$NH$_3$SnI$_3$ perovskite solar cells with high efficiency. *Chin. Phys. B* **2016**, *25*, 108802–188809. [CrossRef]

68. Singh, P.; Ravindra, N.M. Temperature dependence of solar cell performance—An analysis. *Sol. Energy Mater. Sol. Cells* **2012**, *101*, 36–45. [CrossRef]